Modeling Dual Reflux-Pressure Swing Adsorption processes: numerical solution based on the Finite Volume Method

Ester Rossi[a], *Matteo Paloni*[b], *Giuseppe Storti*[c], *Renato Rota*[a,*]

[a] Chemistry, Materials and Chemical Engineering Department "Giulio Natta", Politecnico di Milano, Via Mancinelli 7, 20131 Milan, Italy

[b] Centre de Biochimie Structurale, CNRS UMR 5048, UM, INSERM U 1054, 29 Rue de Navacelles, FR-34090 Montpellier, France

[c] ETH Zürich, Department of Chemistry and Applied Biosciences, Vladimir-Prelog-Weg 1-5/10, HCI F 125, 8093 Zürich, Switzerland

Authors Information

Corresponding Author

*Tel.+39 0223993154. Fax: +39 0223993180. E-mail: renato.rota@polimi.it

Abstract

Even if the suitability of Finite Volume discretization methods for Pressure Swing Adsorption modelling is well-established, when simulating the peculiar process called Dual Reflux-Pressure Swing Adsorption, simulations relying only on Finite Difference discretization methods are available in literature. Therefore, a detailed single-bed model of the Dual Reflux-Pressure Swing Adsorption process, the solution of which is based on the Finite Volume discretization method, is proposed in this work and validated against experimental data. Details of the system representation, the numerical schemes and the implementation of the boundary conditions are given. Moreover, a comparison between the performances and limitations of the Finite Volume and Finite Difference discretization methods when simulating a Dual Reflux-Pressure Swing Adsorption process are discussed through two case studies, leading to conclude that Finite Volume Method is the most effective approach for simulating this specific separation process.

Keywords

Pressure Swing Adsorption; Dual-reflux; Gas separation; Cyclic adsorption process; Finite Volume Method; Finite Difference Method.

https://doi.org/10.1016/j.ces.2019.03.055

Symbols

A	Heavy component
a_i	First Langmuir coefficient of component i
B	Light component
b_i	Second Langmuir coefficient of component i
BD	Blowdown step
C	Capacity Ratio
D_L	Diffusivity coefficient $[m^2/s]$
D_{bed}	Diameter of the adsorption bed
d_p	Diameter of the solid particles
e	Error in the purity prediction
f	Variable flowing through the finite volume walls
FE	Feed step
G	Reflux ratio
H	Linear isotherm constant
k_{bk}	Blake-Kozeny constant
$\bar{k}_{bk}$	Blake-Kozeny constant, dimensionless
k_{LDF}	Linear Driving Force constant
L_{bed}	Bed length
N	Number of computational nodes
n	n^{th}computational node
$\dot{n}$	Molar flowrate
n_{feed}	Computational node corresponding to the lateral feed injection position
$\dot{n}_{feed}$	Lateral feed flowrate

https://doi.org/10.1016/j.ces.2019.03.055

$\dot{n}_H$ Heavy component flowrate $\dot{n}_H = \dot{n}_{HP} + \dot{n}_{HR}$

$\dot{n}_{HP}$ Heavy product flowrate

$\dot{n}_{HR}$ Heavy recycle flowrate

$\dot{n}_L$ Light component flowrate $\dot{n}_L = \dot{n}_{LP} + \dot{n}_{LR}$

$\dot{n}_{LP}$ Light product flowrate

$\dot{n}_{LR}$ Light recycle flowrate

P Pressure

$\bar{P}$ Pressure, dimensionless

P^* Set pressure

PR Pressurization step

PU Purge step

q_i Amount of i on the solid adsorbent

$\bar{q}_i$ Amount of i on the solid adsorbent, dimensionless

q_i^* Amount of i on the solid adsorbent in equilibrium conditions

R Ideal gas constant

r Indicator of smoothness of a variable f

R_L Light recycle ratio

r_p Particle radius

S State variables vector, dimensionless

s State variable, dimensionless

$\boldsymbol{s}$ Averaged state variable, dimensionless

T Temperature

t Time

$\bar{t}$ Time, dimensionless

https://doi.org/10.1016/j.ces.2019.03.055

t_c Computational time

u Superficial velocity

$\bar{u}$ Superficial velocity, dimensionless

$y_{i,feed}$ Molar fraction of i in the lateral feed injection flow

$y_{i,H}$ Average molar fraction of i in ϑ_2

$y_{i,L}$ Average molar fraction of i in ϑ_1

y_i Molar fraction of i

z_{feed} Feed injection position, dimensionless

z_{feed}^- z coordinate of the outlet of Bed 1 Bottom

z_{feed}^+ z coordinate of the inlet of Bed 1 Top

z Axial coordinate, dimensionless $z = Z/z_{rif}$

Z Axial coordinate

Greek symbols

ε_{MB} Error on the material balance

ε_{MB_i} Error on the single component material balance

ϵ_B Bed void fraction

ϵ_T Total void fraction

ϵ_P Solid particles porosity

ϕ Flux limiter

ρ_s Solid density

ρ_B Bed density

μ Dynamic viscosity

π High pressure to low pressure ratio

https://doi.org/10.1016/j.ces.2019.03.055

ϑ_1 Tank 1

ϑ_2 Tank 2

τ Dimensionless computational time

Acronyms

PSA	Pressure Swing Adsorption
DR-PSA	Dual Reflux-Pressure Swing Adsorption
FVM	Finite Volume Method
FDM	Finite Difference Method
PDE	Partial Differential Equation
ODE	Ordinary Differential Equation
PR	Pressurization step
FE	Feed step
PU	Purge step
BD	Blowdown step
RAM	Random Access Memory
TVD	Total Variation Diminishing
CSS	Cyclic Steady State
IC	Initial Condition
BC	Boundary Condition

Subscripts

i Component i, $i = A$ or B

n n^{th} computational node, $n = 1 \dots N$

A Heavy component

https://doi.org/10.1016/j.ces.2019.03.055

B	Light component
rif	Reference value
$n \pm \frac{1}{2}$	Walls of the computational nodes n
BD	Blowdown step
ET	Equilibrium Theory
FE	Feed step
PR	Pressurization step
PU	Purge step
H	Highest value of the cycle
L	Lowest value of the cycle
max	Maximum value
min	Minimum value

https://doi.org/10.1016/j.ces.2019.03.055

1. Introduction

The recovery of pure components from chemical mixtures is a crucial step in most typical processes of the chemical industry (Sholl and Lively, 2016). The separation processes currently most used account for 10–15% of the process industry's energy consumption, thus channelling research efforts towards those which have the potential to be cost-reducing (less energy intensive). Among the many alternatives, adsorption separations have attracted much interest in recent years. These processes exploit the different affinity of the components for a solid adsorbent. Even though adsorption separations are usually more expensive than well-assessed processes like distillation, absorption and extraction, in many cases they have become an attractive option, especially when the components are chemically similar, thus exhibiting minor differences in terms of boiling or melting temperatures (Ruthven, 1984).

In the frame of adsorption processes involving gaseous binary systems, solid regeneration can be effectively performed by reducing the total pressure of the system; the process is known as Pressure Swing Adsorption (PSA). Namely, the system pressure "swings" from a high value during the feed step (FE) to a low value during the regeneration step (also known as the purge step (PU)) (Grande and Blom, 2012). The vast majority of PSA systems are of "stripping type" (Skarstrom, 1959), which means they are capable of producing only the light product at high purity from a binary feed gas mixture, or a "rectifying type" (Diagne et al., 1994; Ebner and Ritter, 2002), *i.e.*, capable of producing only the heavy product at high purity (Bhatt et al., 2013). Therefore, PSA processes, based on the conventional cycles, cannot produce both products at high purity regardless of the high-to-low pressure ratio (Yoshida et al., 2003), particularly when the selectivity between the two components is poor (May et al., 2017).

To overcome this limitation, new configurations have been proposed. Specifically, an attractive solution capable of achieving both products at high purity is the combination of the aforementioned stripping and rectifying PSA into a single two-bed system with feed gas admitted to an intermediate position along the axis of the adsorbent bed. In addition to this lateral feed injection, two reflux streams are also applied, thus determining the name: Dual Reflux-PSA (DR-PSA). The product streams of the resulting process are no longer affected by the thermodynamic limits mentioned above for the standard PSA processes and high purity streams, up to complete separations, can be achieved. Four different DR-PSA cycle configurations have been proposed in the literature, differentiated by the operating pressure of the bed at which the feed gas is admitted and by which one of the two product streams, light- or heavy-rich, is employed to perform the process steps at variable pressure, PR and BD steps (Kearns and Webley, 2006a). Starting from these basic configurations, modified or even more

https://doi.org/10.1016/j.ces.2019.03.055

complicated DR-PSA configurations have been proposed more recently, such as those proposed by (Sivakumar and Rao, 2011a; Sivakumar and Rao, 2011b) aiming at process intensification.

In order to explore the features of DR-PSA as well as to design and optimize the corresponding separation process, different approaches have been reported in the literature, involving both experimental (Mc Intyre et al., 2002; Mcintyre et al., 2010; Saleman et al., 2015) and modelling activity (Bhatt et al., 2014; Diagne et al., 1995; Li et al., 2016).

Focusing on the modelling works, the mathematical models proposed to simulate DR-PSA are quite different in terms of complexity (Bhatt et al., 2017). In the simplest case, the process simulation is carried out using a model involving several assumptions and based on the so-called Equilibrium Theory. This approach was first applied to DR-PSA by Ebner and Ritter (Ebner and Ritter, 2004) and exploited in later works to study and optimize the separation process (Kearns and Webley, 2006a; Bhatt et al., 2015; Bhatt et al., 2017). The main assumptions underlying the analytical solution developed through the Equilibrium Theory are: (i) instantaneous equilibrium between gas and solid phases, (ii) linear equilibrium isotherms, (iii) ideal gas behaviour, (iv) complete separation of a binary mixture, (v) ideal plug flow (no axial mixing), (vi) isothermal operation, and (vii) negligible pressure drop (constant pressure along the column axis).

Another possibility is the development of a detailed model overcoming most of the assumptions mentioned above, thus enabling a more reliable description of the process. Owing to the nature of the conservation equations describing the DR-PSA process, sharp fronts of concentration may propagate along the adsorption column. Therefore, ensuring accuracy and stability of the simulation code that solves the corresponding model equations numerically is quite challenging (Haghpanah et al., 2013). Moreover, It should be noted that the presence of the two refluxes makes the dynamics of the two columns strongly coupled, further complicating the numerical solutions of the corresponding models.

When a detailed model is developed, the most difficult task is to identify the best compromise between contrasting requirements: (i) detailed equations, to capture all main process features, (ii) flexible modelling approach, to be easily adapted to different process configurations, and (iii) simple enough solution algorithm, to limit the computational effort associated with its numerical solution. In particular, the conservation equations governing an adsorption process are invariably gathered in a system of coupled non-linear Partial Differential Equations (PDEs) the effective numerical solution of which is definitely non-trivial. Different numerical approaches are available to solve this type of PDEs, such as: moving and fixed finite element methods (Baines, 1994; Coimbra et al., 2016), finite difference schemes relying on moving grids, combinations of finite difference with method of characteristics,

https://doi.org/10.1016/j.ces.2019.03.055

orthogonal collocations, Finite Volume Methods (FVM), and others (Webley and He, 2000). In spite of this, the Finite Difference Method (FDM) was the only one used to simulate the peculiar DR-PSA processes until now (Sivakumar and Rao, 2011a; Sivakumar and Rao, 2011b; Thakur et al., 2011; Zhang et al., 2016; Zhang et al., 2014; Li et al., 2016; May et al., 2017; Tian et al., 2017; Zou et al., 2017). This is quite surprising considering that in the DR-PSA process the dynamics of the two columns are strongly coupled by the two refluxes, and that the lateral injection of the feed stream (not present in the standard PSA configurations) leads to specific interactions with the waves traveling through the bed. The resulting behavior is quite complex (therefore making the numerical solution of the mathematical model quite complex too) and cannot be easily predicted based on the results on single-column systems without the lateral feed previously reported in the literature. Even for much simpler PSA processes, only one paper compared (in a very implicit way) the performances of FVM vs. FDM for a conventional VSA process (Haghpanah et al., 2013). However, process conditions leading to smooth concentration profiles were investigated, thus making the achievement of grid-independent results quite easy with both methods. It should also be noted that in the literature a single bed is always simulated while going through the entire sequence of steps required by a DR-PSA cycle, which is viable once it is assumed that the two beds are identical (hereinafter referred to as *single-bed approach*).

Notably, the FVM (Webley and He, 2000) has never been used to simulate the complex DR-PSA process and, therefore, no comparative evaluation has been reported in the literature assessing the performances of different numerical approaches for DR-PSA units. Moreover, alternative simulation approaches (with regards to the aforementioned single-bed one) have never been investigated for the complex DR-PSA process. In particular, two beds undergoing simultaneous different process steps could be simulated together; in the following, this approach will be referred to as *double-bed approach*.

According to the short review reported above, in this work we propose a *single-bed approach* combined with a numerical solution of the corresponding differential equations based on the FVM. The resulting approach is first validated by comparison with experimental data from the literature. Then, the performances, in terms of accuracy of the simulation results as well as corresponding computational demand, is compared with those of an FDM-based *single-bed approach,* once again from the literature, as well as with those of an FDM-based *double-bed approach* which was specifically developed. The focus of this work is therefore on the effectiveness of the FVM numerical method.

https://doi.org/10.1016/j.ces.2019.03.055

2. Process configuration and mathematical model

Among the different process configurations (Kearns and Webley, 2006b), let us consider the so-called DR-PH-A cycle, the schematic representation of which is provided in Figure 1a. In this case, each of the two identical adsorption beds (Bed 1 and Bed 2) goes through a cyclical process consisting of four steps. Two of the four steps of each cycle are simultaneously performed at constant pressure, while the other two at variable pressure. The time schedule of the complete cycle is shown in Figure 1b, while Figure 1a represents only half of the complete cycle since the second half is exactly the same after replacing Bed 1 with Bed 2. The lateral feed injection, the position of which in terms of dimensionless axial coordinate z is identified as z_{feed}, divides each adsorption bed into two sections. The section above the feed position ($z > z_{feed}$) is named *Stripping* section, while the one below ($z < z_{feed}$) is named *Rectifying* section.

a)

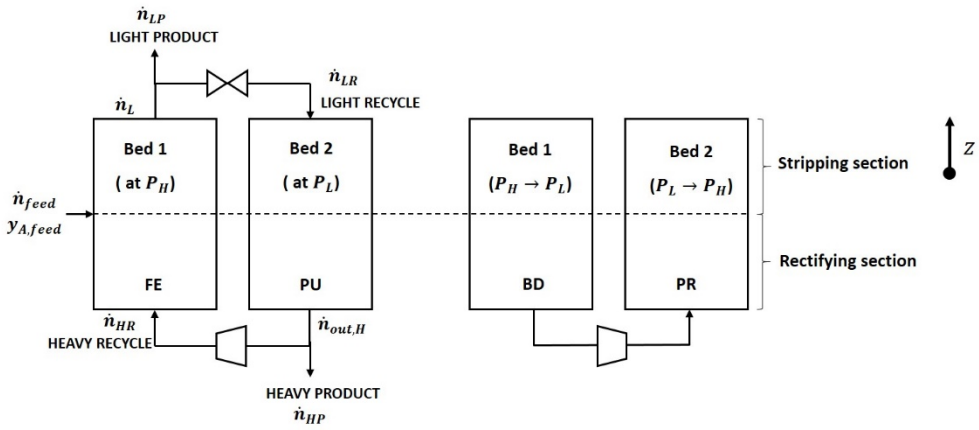

b)

Step duration	t_{FE}	t_{BD}	t_{FE}	t_{BD}
Bed 1	FE	BD	PU	PR
Bed 2	PU	PR	FE	BD
Pressure	P const	$P(t)$	P const	$P(t)$

Figure 1: a) DR-PH-A configuration scheme, b) Time scheduling with corresponding pressure over time behaviour of the DR-PH-A process. Notice that $t_{BD} = t_{PR}$ and $t_{FE} = t_{PU}$.

Also shown in Figure 1a, a binary gas mixture with flowrate $\dot{n}_{feed}$ and molar fraction of component A equal to $y_{A,feed}$ is fed to Bed 1 at z_{feed}, which undergoes the feed step (FE) at a constant pressure equal to P_H. Simultaneously, Bed 2 undergoes the purge step (PU) working at constant pressure P_L. A stream enriched by component B is extracted from Bed 1 with molar flowrate $\dot{n}_L$, of which the fraction $\dot{n}_{LP}$ is withdrawn as light product and the portion $\dot{n}_{LR}$ is recycled to Bed 2 as light recycle. A stream

https://doi.org/10.1016/j.ces.2019.03.055

enriched by component A leaves Bed 2 with flow rate $\dot{n}_{out,H}$, which is then split into the heavy product extracted with flowrate $\dot{n}_{HP}$ and the heavy recycle is sent to Bed 1 with flowrate $\dot{n}_{HR}$. After performing FE and PU steps simultaneously, the two beds undergo the pressure switch. Namely, a gas stream enriched by component A is withdrawn from the rectifying section of Bed 1 and injected into Bed 2. Therefore, Bed 1 undergoes the blowdown step (BD), reducing its pressure from P_H to P_L, while Bed 2 undergoes the pressurization step (PR) rising its pressure from P_L to P_H.

In practical terms, the process in Figure 1 can be implemented as sketched in Figure 2, employing two additional vessels the volume of which is large enough to dampen possible oscillations/irregularities of the inlet flowrate and to avoid artificial mass transfer through FE/PU and BD/PR steps required to fulfil the material balances at Cyclic Steady State (CSS) (Sivakumar and Rao, 2011a). The light component is withdrawn from the top of the high-pressure bed and collected in the high-pressure tank called ϑ_1. Two streams with the same composition leave this tank, one is the light product, $\dot{n}_{LP}$, while the other, $\dot{n}_{LR}$, is recycled to the top of the column at low pressure P_L. The heavy component is then withdrawn from the bottom of the beds purging and undergoing BD and collected in the low pressure tank ϑ_2, from which three streams branch off: the heavy product, $\dot{n}_{HP}$, the heavy reflux, $\dot{n}_{HR}$, sent to the bottom of the high-pressure bed, and the stream used for pressurising Bed 2, $\dot{n}_H$.

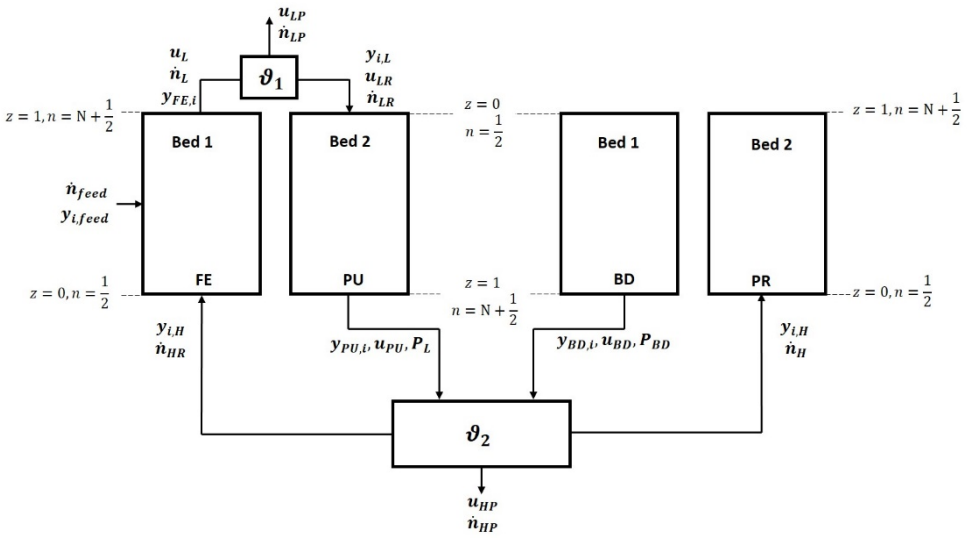

Figure 2: Process detailed representation

The main assumptions underlying the developed DR-PSA model are the following:

- The gas obeys the ideal gas law;
- The process is isothermal;
- The mass transfer between solid and gas phases is represented by the Linear Driving Force (LDF) model (Farooq et al., 1989);

https://doi.org/10.1016/j.ces.2019.03.055

- The pressure drops along the columns are estimated through the Blake-Kozeny equation (Thakur et al., 2011);
- Axial dispersion is neglected, given the very large values of the axial Peclet number, typical of these units (Liao and Shiau, 2000).

Under these assumptions, the dynamics of each adsorption bed are simulated by the following set of PDEs:

$$\epsilon_T \frac{\partial P}{\partial t} + \frac{\partial (uP)}{\partial z} + \rho_B RT \sum_{i=1}^{2} \frac{\partial q_i}{\partial t} = 0 \quad (1)$$

$$\epsilon_T \frac{\partial (Py_i)}{\partial t} + \frac{\partial (uPy_i)}{\partial z} + RT\rho_B \frac{\partial q_i}{\partial t} = 0 \quad (2)$$

$$\frac{\partial q_i}{\partial t} = k_{LDF,i}(q_i^* - q_i) \quad (3)$$

$$\frac{\partial P}{\partial z} = -\frac{u}{k_{bk}}. \quad (4)$$

These equations represent the total material balance (Eq. (1)), the material balance of component i (Eq. (2)), the material balance of the same component in its solid phase (Eq. (3)) and the Blake-Kozeny equation used to evaluate the pressure drops along the unit (Eq. (4)), for a single bed. The last equation is used to evaluate the velocity profile along the column axis. Other formulations, such as the Ergun equation, could be used for this purpose, which would be more appropriate when the velocities in the bed are larger as for example in the BD and PR steps. However, by properly setting a BD/PU step elapsed time large enough to guarantee low velocities across the bed, the Blake-Kozeny equation adequately represents the pressure over z behaviour. Finally, the concentration of the adsorbed species i at equilibrium conditions, q_i^*, will be expressed as a function of P and y_i through a suitable equilibrium isotherm. For example, in the case of Langmuir isotherm (Ruthven, 1984), Eq. (5) applies:

$$q_i^* = \frac{a_i P y_i}{1 + b_i P y_i} \quad (5)$$

where a_i and b_i are the Langmuir coefficients for species i.

The model is supplemented by the material balances of the vessels. Since the volume of the vessels was assumed large enough, the molar fractions of the streams exiting the vessels correspond to the time-averaged gas molar fraction of the streams entering them. In particular, the molar fraction $y_{i,L}$ of the two streams, $\dot{n}_{LP}$ and $\dot{n}_{LR}$, is computed as a time-averaged gas molar fraction of the stream entered into ϑ_1 in the previous FE step:

https://doi.org/10.1016/j.ces.2019.03.055

$$y_{i,L} = \frac{\int_{t_{0,FE}}^{t_{0,FE}+t_{FE}} \frac{u_L P_H y_{FE,i}}{RT} dt}{\int_{t_{0,FE}}^{t_{0,FE}+t_{FE}} \frac{u_L P_H}{RT} dt} \quad (6)$$

Similarly, the molar fraction $y_{i,H}$ of the three streams exiting ϑ_2, $\dot{n}_{HR}$, $\dot{n}_{HP}$ and $\dot{n}_H$, is obtained by computing the time average molar fraction of the gaseous streams entering the tank during the previous BD and PU steps:

$$y_{i,H} = \frac{\int_{t_{0,BD}}^{t_{0,BD}+t_{BD}} \frac{u_{BD} P_{BD} y_{BD,i}}{RT} dt + \int_{t_{0,PU}}^{t_{0,PU}+t_{PU}} \frac{u_{PU} P_L y_{PU,i}}{RT} dt}{\int_{t_{0,BD}}^{t_{0,BD}+t_{BD}} \frac{u_{BD} P_{BD}}{RT} dt + \int_{t_{0,PU}}^{t_{0,PU}+t_{PU}} \frac{u_{PU} P_L}{RT} dt} \quad (7)$$

The resulting set of equations can be made dimensionless by replacing the dimensional variables u, P and q_i in Eqs. (1-4) with their dimensionless form $\bar{u} = u/u_{ref}$, $\bar{P} = P/P_{ref}$ and $\bar{q}_i = q_i/q_{ref}$, where the subscript ref indicates suitable, constant reference values. Therefore, the system of PDEs governing DR-PSA units is a function of the unknown state variables grouped in vector $S = [\bar{q}_i, y_i, P]$, whose size is $(5,1)$ when considering a binary mixture separation.

Finally, it is worth noting that 7 streams are involved in the considered process: $\dot{n}_{feed}, \dot{n}_H, \dot{n}_{HP}, \dot{n}_{HR}, \dot{n}_L, \dot{n}_{LP}$ and $\dot{n}_{LR}$ (with reference to Figure 2). At CSS, these streams are linked by the material *in-out* balances from each Bed (1 and 2) and tank (ϑ_1 and ϑ_2), gathered in four equations, thus resulting in $7 - 4 = 3$ degrees of freedom for this system. Therefore, we choose to arbitrarily set $\dot{n}_{HP}, \dot{n}_{feed}$ and $\dot{n}_{LR}$.

3. Numerical solution of the single fixed bed: FVM

The FVM is a numerical scheme particularly suitable for modelling hyperbolic conservation laws (Webley and He, 2000). The spatial domain is split into *N* finite volumes of (not necessarily) constant size and Eqs. (1-4) are integrated over each volume element. Under the previous assumptions (see Section 3), any state variable $s(z)$ (the time dependence is neglected for simplicity) is assumed to be constant over a finite interval Δz and its average value, $\boldsymbol{s}_n$, defined as in Eq. (8), is lumped at the centre of the same interval:

$$\int_{n-\frac{1}{2}}^{n+\frac{1}{2}} s(z)dz = \boldsymbol{s}_n \Delta z. \quad (8)$$

Given these values, all spatial derivatives are approximated by cell-centred differences; the resulting discretized equations (each PDE is discretized into N ODEs (Friedrich et al., 2013)) are detailed in Appendix A.

https://doi.org/10.1016/j.ces.2019.03.055

By applying this approach, the spatial domain is reduced to a set of finite "volumes" (actually intervals in the 1D case under examination), as sketched in Figure 3. The discretized equations involve the state variables evaluated at the centre of Δz, indicated in the figure by the subscript n. On the other hand, these same variables depend on the state variables at the walls of the finite volumes, those identified by the subscript $n \pm \frac{1}{2}$ (this same notation is applied in Appendix A). Therefore, in order to evaluate the spatial derivatives of the state variables, the values of the same variables at the finite volume walls have to be determined by interpolation.

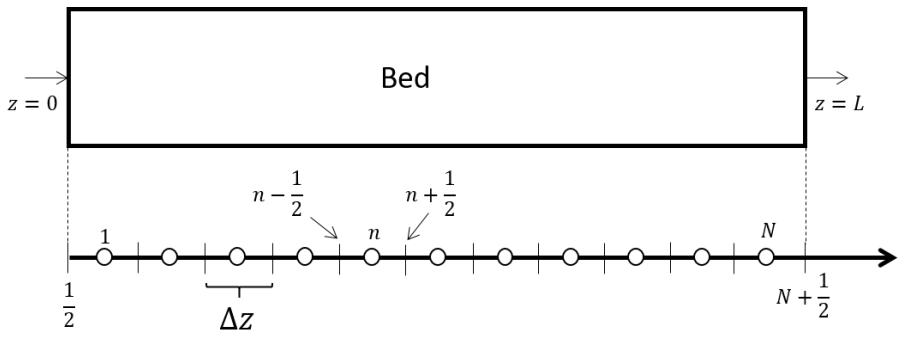

Figure 3: Schematic of adsorption bed and FVM discretization.

The standard formulation of FVM, relying on linear interpolation for estimating wall values, is not suitable in the case under examination. In fact, from a physical viewpoint, the convection of fluid properties from upstream to downstream dominates the transport of species and any numerical approximation should mirror this feature. Moreover, adsorption processes involving gas mixtures are often characterized by very sharp concentration fronts propagating along the adsorption bed. These features suggest we apply conservative interpolation schemes, such as the high-resolution Total Variation Diminishing (TVD) scheme (LeVeque, 2002). The TVD scheme combines the accuracy of higher order schemes with the stability of the lower order ones, enabling us to deal with sharp discontinuities while ensuring accuracy at the same time.

Let us consider the vector $f = [\bar{P}, \bar{u}, y_i]$ collecting all the variables whose wall values have to be interpolated. Notice that $\bar{u}$ is involved even if it is not strictly a state variable; however, as anticipated, it is a function of $\bar{P}$ through the Blake-Kozeny equation. The TVD scheme applied to express the wall value $f_{n\pm\frac{1}{2}}$ gives us Eq. (9):

$$f_{n+\frac{1}{2}} = f_n + \frac{1}{2}\phi\left(r_{n+\frac{1}{2}}\right)(f_{n+1} - f_n) \qquad (9)$$

where

https://doi.org/10.1016/j.ces.2019.03.055

$$r_{n+\frac{1}{2}} = \frac{f_n - f_{n-1} + \delta}{f_{n+1} - f_n + \delta} \quad (10)$$

with $r_{n+\frac{1}{2}}$ representing the ratio of consecutive gradients of f and δ is assumed equal to 10^{-10} in order to prevent the algorithm from diving by zero. ϕ is referred to as the Flux Limiter; among the many possibilities, we have chosen the flux limiter formulation expressed by Van Leer (LeVeque, 2002) whereby ϕ is defined as:

$$\phi_{n+\frac{1}{2}} = \frac{r_{n+\frac{1}{2}} + \left| r_{n+\frac{1}{2}} \right|}{1 + \left| r_{n+\frac{1}{2}} \right|}. \quad (11)$$

By applying Eqs. (9-11), expressing the wall values of f becomes trivial when considering the computational nodes for which the values f_n, f_{n+1} and f_{n-1} are available.

This implementation becomes more complicated when considering boundary cells, for example, $n = \frac{1}{2}$. In this case, to perform the interpolation, the values of f in $n = 0, 1$ and 2 are needed. While the values in $n = 1$ and 2 are known, the values in $n = 0$ are not since it is out of the computational domain (cf. Figure 3). To overcome this problem, a "ghost cell" is usually introduced. On the contrary, in this work we avoid using ghost cells by adopting the half-cell approximation (Haghpanah et al., 2013) which assumes that the difference $(f_{n=1} - f_{n=\frac{1}{2}})$ is equal to $(f_{n=\frac{1}{2}} - f_{n=0})$. Under this assumption, Eq. (12) is as follows:

$$(f_{n=1} - f_{n=0}) = 2(f_{n=1} - f_{n=\frac{1}{2}}) \quad (12)$$

Note that this same half-cell approximation has been applied to all remaining boundaries, $i.e.$, $n = N + \frac{1}{2}$ and at the lateral injection.

4. FVM-based *single-bed approach* for DR-PSA simulation

After presenting the main features of the FVM and its application to the single fixed bed, let us discuss the approach applied to simulate the entire DR-PSA cycle.

Focusing on the single column's behaviour, three different situations are established during the different steps of the cyclical adsorption process: (i) the open-open step, where the stream enters from one end of the adsorption bed and exits through the other; (ii) the open-closed step, where one end of the bed is closed and the other is open to force the pressurizing stream within; and (iii) the closed-open step, which is the same as the open-closed one, but with the flow just leaving the bed

https://doi.org/10.1016/j.ces.2019.03.055

without any inlet stream. This classification applies also to each section of the column at high pressure during the FE step, where two semi-columns are working in series, divided by the lateral feed injection. According to this schematization, FE and PU are steps of the open-open kind, BD is a closed-open step while PR is an open-closed one. Different sets of suitable boundary conditions should be applied in each case (Haghpanah et al., 2013) as summarized in Table 1. In the table, $\bar{u}_{in}$ is the velocity of the inlet stream, while $\bar{P}^*$ is the pressure established at the bed outlet. Note that, in the *single-bed approach*, the axial coordinate z is conveniently set to have the same direction for the FE and PR steps, while the opposite is set for the BD and PU steps. In agreement with the general scheme in Table 1, the complete sets of Initial Conditions (ICs) and Boundary Conditions (BCs) are reported in Appendix B for each process step.

Table 1: Boundary conditions.

Bed position / ***Step***	$\mathbf{z = 0}$		$\mathbf{z = 1}$
Closed-open	$\left.\frac{\partial y_i}{\partial z}\right\|_{z=0} = 0$	$\bar{u}\|_{z=0} = 0$	$\bar{P}\|_{z=1} = \bar{P}(t)$
Open-open	$\left.\frac{\partial y_i}{\partial z}\right\|_{z=0} = 0$	$\bar{u}\|_{z=0} = \bar{u}_{in}$	$\bar{P}\|_{z=1} = \bar{P}^*$
Open-closed	$\left.\frac{\partial y_i}{\partial z}\right\|_{z=0} = 0$	$\bar{P}\|_{z=0} = \bar{P}(t)$	$\bar{u}\|_{z=1} = 0$

Finally, a special aspect of the BD and PR steps has to be mentioned. A compressor is required to complete the depressurization of one bed down to P_L and the pressurization of the other up to P_H. Instead of modelling the compressor itself, this behaviour is taken into account by arbitrarily assigning a pressure or velocity profile over time at the exit of the bed undergoing BD and at the inlet of that undergoing PR, given that the specific pressure profiles are not critical when modelling these steps (Casas et al., 2013).

The ODEs system resulting from the FVM discretization of the spatial domain of Eqs. (1-4), together with the suitable ICs and BCs, has been implemented in Matlab®, version R2017a, using the function *ode15s*. The calculation starts at $\bar{t} = 0$ in BD step, then the PU, PR and finally FE steps are simulated to complete a cycle. At the end of each cycle, the profiles of all state variables are set as initial profiles for the following step, considering the orientation of the axial coordinate. When the simulation of a complete cycle is terminated, the final profile of the FE step is set as initial profile for the next BD step,

https://doi.org/10.1016/j.ces.2019.03.055

which corresponds to the first step of the following cycle. The simulation then continues until CSS is reached.

This FVM-based *single-bed approach* has been validated by comparison with experimental data available in the literature for a DR-PH-A configuration, the separation of N_2/CH_4 (May et al., 2017). The operating conditions as well as the model parameter values are summarized in Table 2 and Table 3. These runs were carried out keeping almost constant the $\dot{n}_{feed}$ values, while changing the $\dot{n}_{LR}$ values. In other words, they correspond to different values of the light recycle ratio $G = \frac{\dot{n}_{LR}}{\dot{n}_{feed}}$.

Table 2: Experimental CSS flowrates (May et al., 2017)

$\boldsymbol{Run}$	$\dot{\boldsymbol{n}}_{\boldsymbol{feed}}[\boldsymbol{SLPM}]$	$\dot{\boldsymbol{n}}_{\boldsymbol{HP}}[\boldsymbol{SLPM}]$	$\dot{\boldsymbol{n}}_{\boldsymbol{LR}}[\boldsymbol{SLPM}]$
27	1.160	0.230	5.009
28	1.151	0.233	4.010
29	1.147	0.238	2.983
30	1.149	0.233	2.042
31	1.147	0.227	1.062

Table 3: Operating conditions and parameters, bed specifics and adsorption equilibrium data (May et al., 2017; Zhang et al., 2016; Saleman et al., 2015)

ε_P	0.65	
ε_B	0.433	
P_H	$5 \cdot 10^5\ Pa$	
P_L	$1.4 \cdot 10^5 Pa$	
y_{feed}	0.104	
T	$298.15\ K$	
ρ_s	$2150\ kg/m^3$	
d_p	$0.003\ m$	
L_{bed}	$0.98\ m$	
D_{bed}	$0.035\ m$	
z_{feed}	0.5	
$k_{LDF,A}$	$1\ s^{-1}$	
$k_{LDF,B}$	$3\ s^{-1}$	
t_{PR}	$90\ s$	
t_{FE}	$120\ s$	
a_i	$IP_{1i} \exp\left(\frac{IP_{2i}}{T}\right)$	
b_i	$IP_{3i} \exp\left(\frac{IP_{4i}}{T}\right)$	
	A	B
IP_1	$6.58 \cdot 10^{-7}\ kmol\ kg^{-1} bar^{-1}$	$7.3 \cdot 10^{-7}\ kmol\ kg^{-1} bar^{-1}$
IP_2	$2077\ K$	$1722\ K$
IP_3	$1.19 \cdot 10^{-4}\ bar^{-1}$	$1.75 \cdot 10^{-4}\ bar^{-1}$
IP_4	$2077\ K$	$1722\ K$

https://doi.org/10.1016/j.ces.2019.03.055

The experimental runs in Table 2 have been simulated by adopting a spatial grid of 50 computational nodes and using a machine equipped with an Intel® Core™ i5 1.60 GHz processor. A grid sensitivity analysis has been initially carried out, showing that an increase in the number of computational nodes does not affect the simulation results. With the selected number of grid points, the computational time was about 20 min for a typical run.

Experimental and simulation results are compared in Figure 4, in terms of heavy and light component purities at CSS.

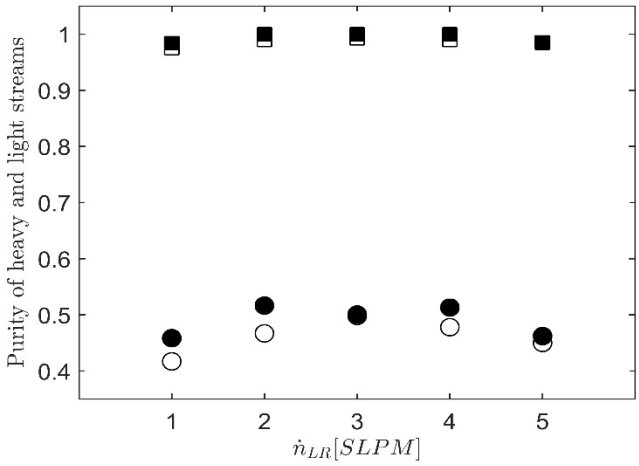

Figure 4: Purities at CSS of heavy (circles) and light (squares) streams: FVM single-bed approach (full symbols) and experimental data (empty symbols; May et al., 2017).

The simulated data shows substantial agreement with the experimental ones for both light and heavy purities. A minor discrepancy can be found in the trend of the heavy component purity, which, according to the experimental results, should show a maximum near the operating conditions of Run 29. This discrepancy may be due to experimental uncertainties on the flowrate measurement leading to erroneous fluctuations in the $\dot{n}_{feed}$ and $\dot{n}_{HP}$ values (May et al., 2017). To reduce the effect of this uncertainty on the simulated results, all the simulations at variable values of the light reflux flowrate $\dot{n}_{LR}$ have been repeated enforcing constant, averaged values for $\dot{n}_{feed}$ and $\dot{n}_{HP}$. In this case, the experimental data is compared with the model predictions in Figure 5, again in terms of heavy and light component purities at CSS. Smoothing the experimental uncertainties in the input data leads to a slightly improved qualitative agreement between experimental and simulated results.

https://doi.org/10.1016/j.ces.2019.03.055

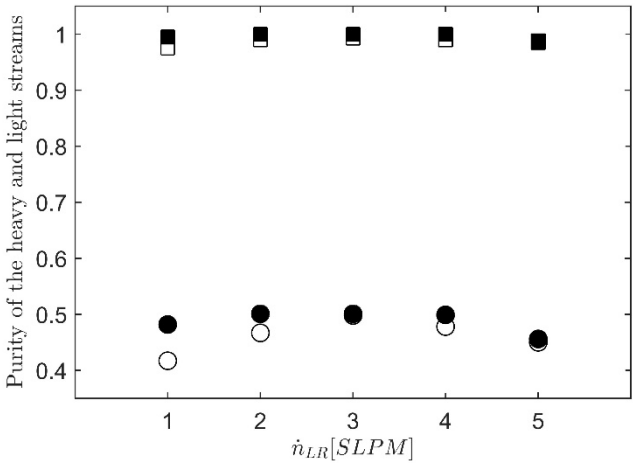

Figure 5: Purities at CSS of heavy (circles) and light (squares) streams: FVM single-bed approach (full symbols; constant averaged values of $\dot{n}_{feed}$ and $\dot{n}_{HP}$) and experimental data (empty symbols; May et al., 2017).

5. Case study 1: Comparison with FDM-based single-bed approach

As mentioned above, all the previous modelling works dealing with the simulation of the DR-PSA process applied the FDM-based *single-bed approach* for the numerical solution. Among others, the aforementioned paper by May et al., (2017) also reports the results of a detailed simulation model using this approach, thus allowing a direct comparative evaluation of the previously discussed FVM-based *single-bed approach*. All the details on the mathematical model and numerical methods applied in the literature can be found in the corresponding publications (May et al., 2017; Zhang et al., 2016).

The differences between the assumptions behind the model implemented by May et al. (2017) and that reported in Section 2 require a preliminary discussion.

First of all, the momentum balance and the pressure drops are described by May et al. (2017) with the Ergun Equation, while we consider the Blake Kozeny equation as suitable for this frame. The two, Ergun and Blake Kozeny, equations can be considered equivalent in our operating conditions since the velocities are very low. In fact, in these conditions, the maximum ΔP along the column, during the FE step, is in the order of a few Pa, which corresponds to 0.002 % of the operating pressure of the step.

Then, the axial dispersion accounted for by May et al. (2017) is neglected in our model, given the values of the axial Peclet number which is typical of these units (Liao and Shiau, 2000).

Finally, isothermal behaviour is assumed in the model discussed in this work while the energy balance is applied in the literature case to evaluate the actual temperature profile inside each column (May et al., 2017). In order to investigate the impact of our last assumption, the influence of the temperature variations experimentally found on the model predictions has been analysed. Namely, the five runs summarized in Table 2 have been simulated, setting once again the temperature equal to either the

https://doi.org/10.1016/j.ces.2019.03.055

lowest or to the largest experimental value. As shown for example in Figure 6 for Run 30, the transient behaviour as well as the steady state values of the purity of component A are almost unaffected varying the temperature from a minimum of 293.15 K to a maximum of 303.15 K, in agreement with the results of the analysis discussed by Zhang et al. (2016). Therefore, we can conclude that the assumption of constant temperature is fully adequate under these conditions and that the results of our isothermal model can be safely compared with those obtained assuming non-isothermal conditions.

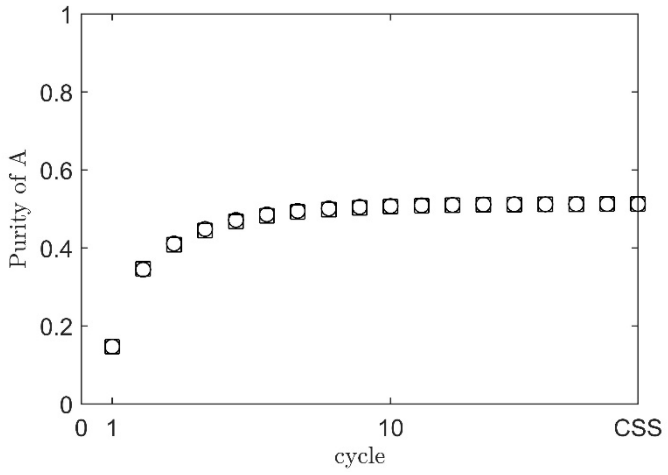

Figure 6: Run 30, FVM single-bed results for purity of A: $T=T_{max}$ (empty circles), $T=T_{min}$ (empty squares).

The comparison between the results of two numerical approaches, FVM and FDM, is shown in Figure 7 in terms of heavy and light product purities at CSS. Even though the results are indeed very similar, it should be mentioned that only the FVM-based results are direct predictions of the mathematical model. In fact, thanks to the computational efficiency of the FVM-based *single-bed approach*, it was possible to use a number of grid points large enough to make the model results independent of the grid size. On the contrary, the number of grid points used in the FDM literature case was limited by the required computational time, leading to results that are not grid-independent (Zhang et al., 2016). As an order of magnitude, using 50 nodes to discretize the whole column requires about 10 s of computational time when using the FVM and about one order of magnitude larger when using the FDM (May et al., 2017). Moreover, much more than 50 nodes would be required in the FDM case, making the grid-independent simulations practically impossible (Zhang et al., 2016). Accordingly, while the results of the FVM-based *single-bed approach* always fulfil the material balances, the results of the FDM-based *single-bed approach* do not (May et al., 2017). As a matter of fact, the errors in overall and single component material balances, as defined by Eq. (13) and Eq. (14):

https://doi.org/10.1016/j.ces.2019.03.055

$$\varepsilon_{MB} = \left(\frac{\int_{t_0}^{t_{feed}} \dot{n}_{feed} dt - \int_{t_0}^{t_{feed}} \dot{n}_{HP} dt - \int_{t_0}^{t_{feed}} \dot{n}_{LP} dt}{\int_{t_0}^{t_{feed}} \dot{n}_{feed} dt} \right) \cdot 100 \quad (13)$$

$$\varepsilon_{MB_i} = \left(\frac{\int_{t_0}^{t_{feed}} \dot{n}_{feed} y_{i,feed} dt - \int_{t_0}^{t_{feed}} \dot{n}_{HP} y_{i,H} dt - \int_{t_0}^{t_{feed}} \dot{n}_{LP} y_{i,L} dt}{\int_{t_0}^{t_{feed}} \dot{n}_{feed} dt} \right) \cdot 100 \quad (14)$$

were smaller than 0.1% for all simulated runs without the need for any correction or error redistribution when using FVM. This was not the case for the FDM results, where the reported average error is 0.34% for total material balance and 2.71% for CH_4 material balance, therefore requiring (arbitrary) reconciliation of the model results in order to force them to fulfil the material balances (Zhang et al., 2016).

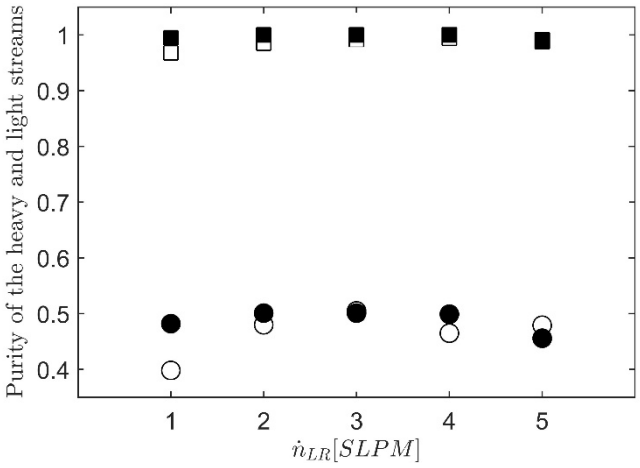

Figure 7: Purities at CSS of heavy (circles) and light (squares) stream: FVM (full symbols) and FDM (empty symbols; May et al., 2017), both in the single-bed approach

6. Case study 2: Comparison with FDM-based double-bed approach

In the previous section, the general performances of the proposed FVM-based *single-bed approach* have been evaluated in comparison with the most popular literature approach, i.e. FDM-based *single-bed approach*. Given the superior performances of the first approach, a different solving algorithm has been implemented in the second case (FDM-based) to check if better performances could also be achieved in this case. Namely, with the aim to account for the interplay between the two beds in a more direct way, the simultaneous solution of the two beds was implemented, thus developing an FDM-based *double-bed approach*. This approach differs from the FDM-based *single-bed approach* because it solves the equations representing the two coupled steps (i.e., FE and PU; PR and BD) at the same time. All the details on both the model equations and the application of the numerical method are available as supplementary material.

https://doi.org/10.1016/j.ces.2019.03.055

This second comparison will be carried out considering the challenging conditions represented by the complete separation conditions as designed using the analytical solution based on the so-called Equilibrium Theory (Ebner and Ritter, 2004; Bhatt et al., 2013). Therefore, to simulate the process in conditions that are consistent with the assumptions underlying the analytical solution (linear adsorption equilibrium, negligible mass transfer limitations, no axial dispersion and pressure drops), the model parameter values have been properly adjusted. Namely:

- The mass transfer coefficients are large enough to represent negligible mass transfer resistances;
- The particle diameter d_p is large enough to ensure negligible pressure drops;
- The axial mixing coefficient is equal to zero.

All the remaining model parameter values are summarized in Table 4, while the process operating conditions, evaluated through the previously mentioned analytical approach (Bhatt et al., 2013), are reported in Table 5.

Table 4: Operating parameters for the second case study.

Operating Parameter	Value
P_H	$2 \cdot 10^5\ Pa$
P_L	$1 \cdot 10^5\ Pa$
$y_{A,feed}$	0.79
T	$303\ K$
ρ_s	$3\,310\ \frac{kg}{m^3}$
d_p	$2 \cdot 10^{-3}\ m$
ϵ_p	0.65
ϵ_B	0.31
μ_{mix}	$1.8 \cdot 10^{-5}\ Pa \cdot s$
L_{bed}	$1\ m$
D_{bed}	$0.03\ m$
t_{PR}	$250\ s$
H_A	$2.3 \cdot 10^{-6}\ \frac{mol}{kg \cdot Pa}$
H_B	$1.0 \cdot 10^{-6}\ \frac{mol}{kg \cdot Pa}$

Table 5: Process parameters given by the Equilibrium Theory for the process with operating parameters summarized in Table 4.

PROCESS PARAMETER	***VALUE***
$\dot{n}_{HP}$	$1.44 \cdot 10^{-5}\ \frac{mol}{s}$
$\dot{n}_{LR}$	$2.25 \cdot 10^{-5}\ \frac{mol}{s}$
$\dot{n}_{feed}$	$1.83 \cdot 10^{-5}\ \frac{mol}{s}$
z_{feed}	0.86
t_{FE}	$400\ s$

https://doi.org/10.1016/j.ces.2019.03.055

The complete separation, to be expected according to the *Equilibrium Theory* prediction, is obtained when adopting the FVM-based *single-bed approach* while this is not the case when using the FDM-based *double-bed approach*. This can be observed in further detail in Figure 8, where the CSS axial profiles of y_A predicted at the end of each process step for both of the approaches using the same number of nodes (300) are shown, and where the dashed curves represent the results obtained with the FVM-based *single-bed approach* while the continuous ones those obtained with the FDM-based *double-bed approach*. The FVM-based approach is able to capture the sharp fronts expected at these conditions much more effectively, thus enabling the two concentration waves to be kept within the corresponding section of the bed, resulting in the expected complete separation. On the contrary, the profiles predicted using the FDM-based double-bed approach are affected by an extensive broadening due to numerical diffusion (Fox, 1996), leading to purity values as low as around 95 %.

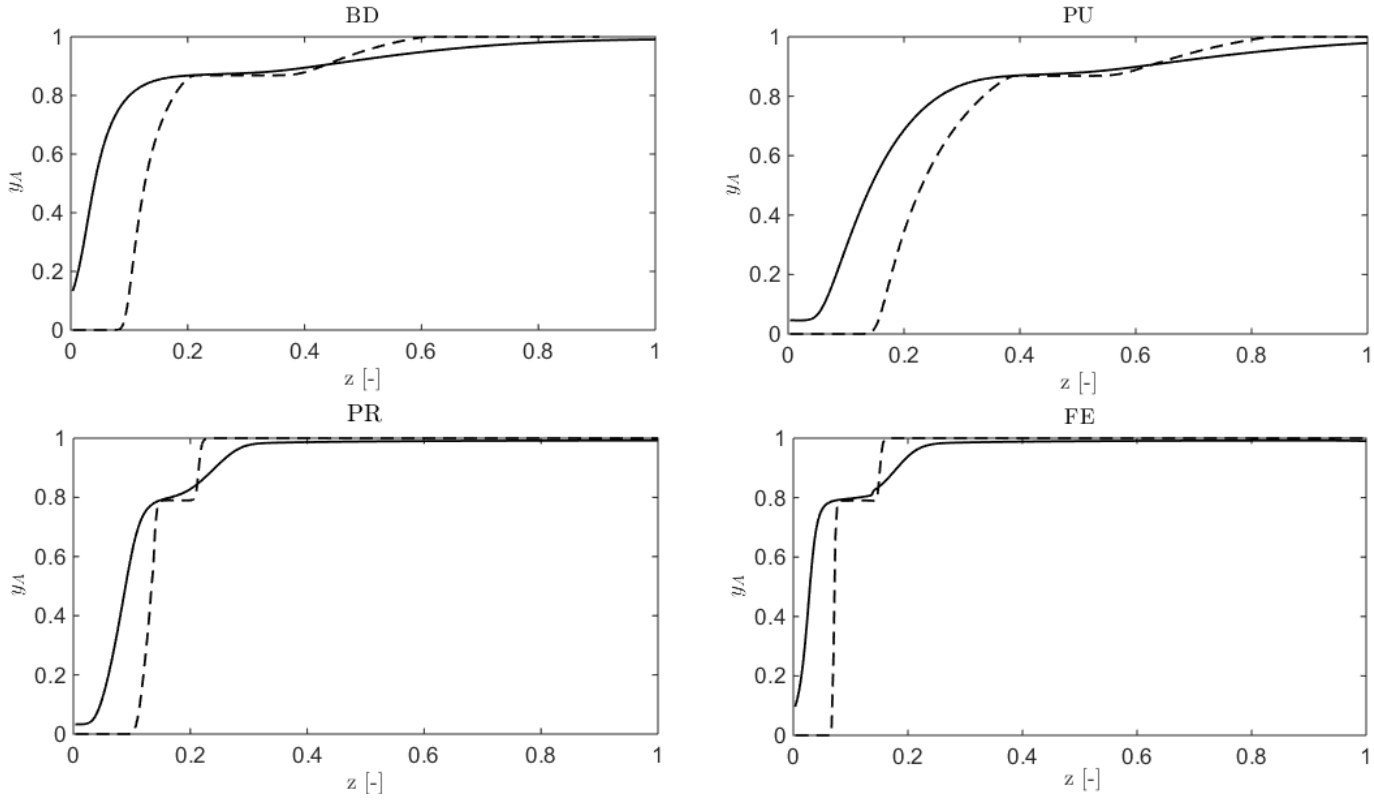

Figure 8: Heavy gas molar fraction profiles along the dimensionless axial coordinate at the end of the various steps, at CSS for the second case study. (--) FVM-based single-bed approach. (-) FDM-based double-bed approach.

Then, to better assess the comparison between the two approaches, a grid sensitivity analysis was carried out the results of which are summarized in Figure 9. In Figure 9a, the purity of the less adsorbable component is reported as a function of the number of grid points, *N*: a value close to 100% corresponds to an accurate numerical solution. While this value is well predicted to already be at *N* =

https://doi.org/10.1016/j.ces.2019.03.055

100 in the FVM-based *single-bed approach*, more than 700 computational nodes would be required when using the FDM-based *double-bed approach*, making the corresponding simulation tool impractical. When using the FVM-based *single-bed approach* and 100 grid points, about $12\,s$ of computational time are required to simulate a process cycle, corresponding to less than 10 min to reach CSS conditions. The values of the computational times required with both of the approaches are reported in dimensionless form in Figure 9b as a function of the number of grid points. All values have been normalized with respect to the time required in the FVM-based *single-bed approach* when using 300 grid points, $i.e.$, $\tau = t_c/70\ s$. While the computational effort grows with the number of grid points in both cases, the superior performances of the FVM-based *single-bed approach* are clear.

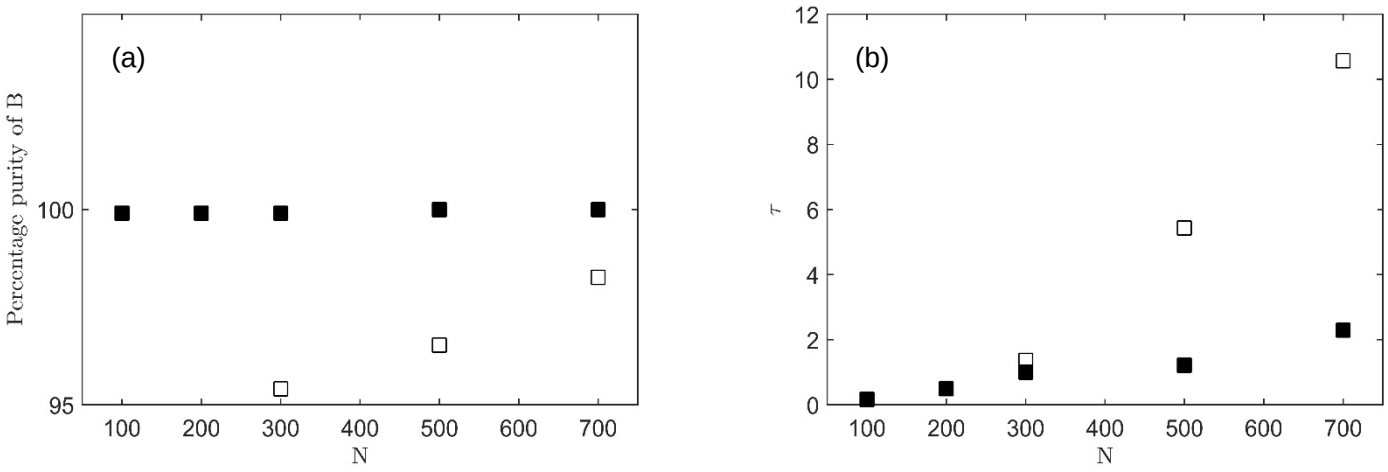

Figure 9: (a) Purity of B in the FE step at CSS; (b) dimensionless computational time as a function of the number of computational nodes. (full squares) FVM-based single-bed approach; (empty squares) FDM-based double-bed approach.

This is even more evident looking at the results in Figure 10, which shows the error vs. the number of computational nodes. The error is defined as the norm with respect to the results of the Equilibrium Theory:

$$e = \left| y_{B,ET} - y_{B,model} \right| \times 100 \qquad (15)$$

where $y_{B,ET}$ is the purity of the light component predicted by the *Equilibrium Theory*, and $y_{B,model}$ is the same quantity predicted by the numerical model. In the figure such an error is plotted as a function of the number of computational nodes, N, for both FVM and FDM. Note that e for the FVM is reported at smaller values of computational nodes than for the FDM given its much larger rate of decrease in error, more than linear in the FVM case and almost linear in the FDM one.

https://doi.org/10.1016/j.ces.2019.03.055

Moreover, from the same figure we can also see that the two methods provide almost the same error when using 50 nodes with FVM and 500 nodes when using FDM; the ratio of the computational time required by the two methods for these two computations is equal to about 20.

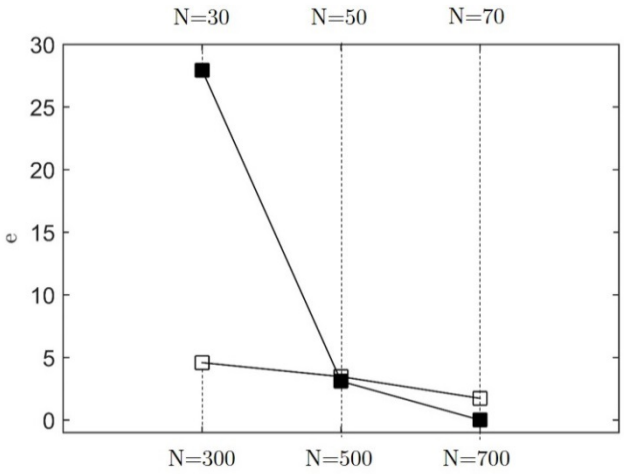

Figure 10: Error, e, as a function of the number of computational nodes N for both FVM- (full squares, top horizontal scale) and FDM-based (empty squares, bottom horizontal scale) approaches.

7. Conclusions

Relying on the FVM for spatial discretization, a numerical approach for a single-bed detailed model of DR-PSA units in a DR-PH-A configuration has been presented. Specifics of the numerical approach, boundary conditions and particular features, such as the lateral feed injection modelling, have been discussed. The proposed approach has been validated against some experimental data from the literature and then compared with other process representations through two case studies. In particular, we focus at first on the *single-bed approach*, and in this frame we compare the performances of our FVM-based approach and those of an FDM-based one available in the literature. The comparison, made in terms of purity prediction and computational performances for conditions involving non-linear adsorption isotherms and non-complete separation of a binary mixture, leads to the conclusion that the FVM based approach is more effective in DR-PSA applications. Secondly, we further assess the proposed numerical strategy by comparison with a different numerical approach, an FDM-based *double-bed approach*. This comparison was carried out considering, as a case study, the numerically demanding complete separation of a binary mixture exhibiting linear adsorption isotherms approaching equilibrium conditions. Also in this case, the FVM-based *single-bed approach* allows for reliable results, despite the very sharp concentration profiles developed through the columns at the selected operating conditions. The computational effort associated with the proposed approach is quite limited (coarse grids are needed), making this methodology the best one when an extensive use of the modelling tool is required, which is often the case in process design.

https://doi.org/10.1016/j.ces.2019.03.055

Appendix A

Dimensionless form of the FVM based single-bed model equations

Eqs. (A.1-A.5) are the discretized version of Eqs. (1-4), obtained applying the FVM, where $n = 1 \dots N$.

Total mass balance

$$\frac{\partial \bar{P}_n}{\partial \bar{t}} = c_1 \left(\bar{u}_{n-\frac{1}{2}} \bar{P}_{n-\frac{1}{2}} - \bar{u}_{n+\frac{1}{2}} \bar{P}_{n+\frac{1}{2}} \right) - c_2 \left(\frac{\partial \bar{q}_{1,n}}{\partial \bar{t}} + \frac{\partial \bar{q}_{2,n}}{\partial \bar{t}} \right) \tag{A.1}$$

Component mass balances

$$\frac{\partial y_{1,n}}{\partial \bar{t}} = \frac{c_1}{\bar{P}_n} \left\{ \bar{u}_{n-\frac{1}{2}} \bar{P}_{n-\frac{1}{2}} y_{1,n-\frac{1}{2}} - \bar{u}_{n+\frac{1}{2}} \bar{P}_{n+\frac{1}{2}} y_{1,n+\frac{1}{2}} \right\} - \frac{c_2}{\bar{P}_n} \frac{\partial \bar{q}_{1,n}}{\partial \bar{t}} - \frac{y_{1,n}}{\bar{P}_n} \frac{\partial \bar{P}_n}{\partial \bar{t}} \tag{A.2}$$

$$\frac{\partial y_{2,n}}{\partial \bar{t}} = \frac{c_1}{\bar{P}_n} \left\{ \bar{u}_{n-\frac{1}{2}} \bar{P}_{n-\frac{1}{2}} y_{2,n-\frac{1}{2}} - \bar{u}_{n+\frac{1}{2}} \bar{P}_{n+\frac{1}{2}} y_{2,n+\frac{1}{2}} \right\} - \frac{c_2}{\bar{P}_n} \frac{\partial \bar{q}_{2,n}}{\partial \bar{t}} - \frac{y_{2,n}}{\bar{P}_n} \frac{\partial \bar{P}_n}{\partial \bar{t}} \tag{A.3}$$

Solid phase balances

$$\frac{\partial \bar{q}_{1,n}}{\partial \bar{t}} = c_3 \left(\bar{q}^*_{1,n} - \bar{q}_{1,n} \right) \tag{A.4}$$

$$\frac{\partial \bar{q}_{2,n}}{\partial \bar{t}} = c_4 \left(\bar{q}^*_{2,n} - \bar{q}_{2,n} \right) \tag{A.5}$$

where $\bar{q}^*_i = f(P, y_i)$ is the dimensionless solid phase equilibrium concentration as evaluated by the equilibrium isotherm.

Pressure drops equation:

The pressure drops are described by the dimensionless and discretized form of the Blake-Kozeny equation:

$$\bar{u}_n = \bar{k}_{bk} \left(\bar{P}_{n-\frac{1}{2}} - \bar{P}_{n+\frac{1}{2}} \right) \tag{A.6}$$

where $\bar{k}_{bk} = \frac{P_{rif} k_{bk}}{z_{rif} \Delta \bar{z} u_{rif}}$ is the dimensionless form of the Blake-Kozney equation as previously reminded.

The groups in Eqs. A.1- A.5 are defined as:

$$c_1 = \frac{u_{rif} t_{rif}}{z_{rif} \epsilon_T \Delta \bar{z}} \tag{A.7}$$

https://doi.org/10.1016/j.ces.2019.03.055

$$c_2 = \frac{\rho_B R T q_{rif}}{\epsilon_T P_{rif}} \tag{A.8}$$

$$c_3 = k_{LDF,1} t_{rif} \tag{A.9}$$

$$c_4 = k_{LDF,2} t_{rif} \tag{A.10}$$

The resulting ODEs system is composed by 5 differential equations, in accordance with the dimension of the vector S, for each n^{th} computational node in which the spatial domain has previously been discretized. It leads to a system of $N \times 5$ equations that have to be integrated over time.

https://doi.org/10.1016/j.ces.2019.03.055

Appendix B

The boundary and initial conditions for each process steps are given in the following, accordingly with Table 1.

- *BD step*:

ICs: $\bar{t} = \bar{t}_{0,BD} \rightarrow \bar{P}(\bar{t}_{end,FE}, z), y_i(\bar{t}_{end,FE}, z), \bar{q}_i(\bar{t}_{end,FE}, z)$

BCs: $z = 0 \rightarrow \bar{u}_{\frac{1}{2}} = 0$

$y_{\frac{1}{2}} = y_1$

$z = 1 \rightarrow \bar{P}_{N+\frac{1}{2}} = P(t)/P_{rif}$

The values of $\bar{P}_{\frac{1}{2}}$ and $\bar{u}_{N+\frac{1}{2}}$ are obtained given the values of $\bar{u}_{\frac{1}{2}}$ and $\bar{P}_{N+\frac{1}{2}}$ and knowing that the Blake-Kozeny equation links the velocity with the pressure gradient. In view of the half-cell approximation:

$$\bar{P}_{\frac{1}{2}} = \bar{P}_1 + \frac{\bar{u}_{\frac{1}{2}}}{2\bar{k}_{BK}} \tag{B.1}$$

$$\bar{u}_{N+\frac{1}{2}} = 2\bar{k}_{BK}\left(\bar{P}_N - \bar{P}_{N+\frac{1}{2}}\right) \tag{B.2}$$

Finally, the value of $y_{N+\frac{1}{2}}$ is obtained through a simple first order upwind interpolation:

$$y_{N+\frac{1}{2}} = y_N \tag{B.3}$$

- *PU Step*:

ICs: $\bar{t} = \bar{t}_{0,PU} \rightarrow \bar{P}(t_{end,BD}, z), y_i(\bar{t}_{end,BD}, z), q_i(\bar{t}_{end,BD}, z)$

BCs: $z = 0 \rightarrow \bar{u}_{\frac{1}{2}} = u_{LR}/u_{rif}$

$y_{\frac{1}{2}} = y_{i,L}$

$z = 1 \rightarrow \bar{P}_{N+\frac{1}{2}} = P_L/P_{rif}$

where u_{LR} is obtained by setting the value of R_L. $y_{i,L}$ is computed by using Eq. (B.4) .

$$y_{i,L} = \frac{\int_{\bar{t}_{0,FE}}^{\bar{t}_{0,FE}+\bar{t}_{FE}} \bar{u}_{N+\frac{1}{2},FE} \frac{\bar{P}_H}{RT} y_{i,N+\frac{1}{2},FE} d\bar{t}}{\int_{\bar{t}_{0,FE}}^{\bar{t}_{0,FE}+\bar{t}_{0,FE}} \bar{u}_{N+\frac{1}{2},FE} \frac{\bar{P}_H}{RT} d\bar{t}} \tag{B.4}$$

Eqs. (B.1-B.3) are used to explicit $\bar{P}_{\frac{1}{2}}, y_{i,N+\frac{1}{2}}$, and $\bar{u}_{N+\frac{1}{2}}$.

https://doi.org/10.1016/j.ces.2019.03.055

- *PR Step*:

ICs: $\bar{t} = \bar{t}_{0,PR} \rightarrow \bar{P}(\bar{t}_{end,PU}, z), y_i(\bar{t}_{end,PU}, z), q_i(\bar{t}_{end,PU}, z)$

BCs: $z = 0 \rightarrow \bar{P}_{\frac{1}{2}} = P(t)/P_{rif}$

$y_{\frac{1}{2}} = y_{i,H}$

$z = 1 \rightarrow \bar{u}_{N+\frac{1}{2}} = 0$

$y_{i,H\ PR}$, obtained through Eq. (B.5):

$$y_{i,H} = \frac{\int_{\bar{t}_{0,BD}}^{\bar{t}_{0,BD}+\bar{t}_{BD}} \bar{u}_{N+\frac{1}{2},BD} \frac{\bar{P}_{N+\frac{1}{2},BD}}{R\bar{T}} y_{i,N+\frac{1}{2},BD} d\bar{t} + \int_{\bar{t}_{0,PU}}^{\bar{t}_{0,PU}+\bar{t}_{PU}} \bar{u}_{N+\frac{1}{2},PU} \frac{\bar{P}_{N+\frac{1}{2},PU}}{R\bar{T}} y_{i,N+\frac{1}{2},PU} d\bar{t}}{\int_{\bar{t}_{0,BD}}^{\bar{t}_{0,BD}+\bar{t}_{BD}} \bar{u}_{N+\frac{1}{2},BD} \frac{\bar{P}_{N+\frac{1}{2},BD}}{R\bar{T}} d\bar{t} + + \int_{\bar{t}_{0,PU}}^{\bar{t}_{0,PU}+\bar{t}_{PU}} \bar{u}_{N+\frac{1}{2},PU} \frac{\bar{P}_{N+\frac{1}{2},PU}}{R\bar{T}} d\bar{t}} \quad \text{(B.5)}$$

Eqs. (B.1-B.3) are adapted and used to explicit $\bar{P}_{N+\frac{1}{2}}, \bar{u}_{\frac{1}{2}}$ and $y_{i,N+\frac{1}{2}}$.

- *FE Step*

ICs: $\bar{t} = \bar{t}_{0,FE} \rightarrow \bar{P}(\bar{t}_{end,PR}, z), y_i(\bar{t}_{end,PR}, z), \bar{q}_i(\bar{t}_{end,PR}, z)$

BCs: $z = 0 \rightarrow \bar{u}_{\frac{1}{2}} = u_{HR}/u_{rif}$

$y_{\frac{1}{2}} = y_{i,H}$

$z = 1 \rightarrow \bar{P}_{N+\frac{1}{2}} = P_H/P_{rif}$

The value of u_{HR} is obtained by setting $\dot{n}_{HP}$ and fulfilling the molar balance in vessel ϑ_2. $y_{i,H}$ is equal to $y_{i,H}$, thus computed through Eq. (B.5). Once more, Eqs. (B.1-B.3) are adapted and used to explicit $\bar{P}_{\frac{1}{2}}, \bar{u}_{N+\frac{1}{2}}$ and $y_{i,N+\frac{1}{2}}$.

- *Lateral feed injection*

With reference to Figure B1, z_{feed} falls into an interval Δz between the two successive computational nodes n_{feed} and $n_{feed} + 1$. This axial position is assumed coincident with the element wall separating n_{feed} and $n_{feed} + 1$ and it separates the bed into a bottom semi-column ($[0, z_{feed}^{-}]$) and a top semi-column ($[z_{feed}^{+}, 1]$).

https://doi.org/10.1016/j.ces.2019.03.055

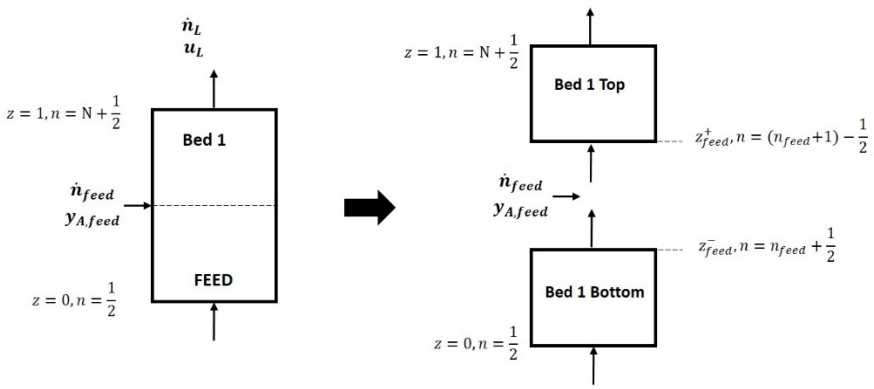

Figure B1: Lateral feed boundary conditions, Approach 2.

The BCs for the two semi-columns are:

$$z = z^{-}_{feed} \quad \rightarrow \quad \bar{P}_{n_{feed}+\frac{1}{2}} = \bar{P}_{(n_{feed}+1)-\frac{1}{2}}$$

$$z = z^{+}_{feed} \quad \rightarrow \quad y_{i.(n_{feed}+1)-\frac{1}{2}} = \frac{y_{i,feed}\bar{u}_{feed}\bar{P}_{feed} + y_{i,n_{feed}+\frac{1}{2}}\bar{u}_{n_{feed}+\frac{1}{2}}\bar{P}_{n_{feed}+\frac{1}{2}}}{\bar{u}_{(n_{feed}+1)-\frac{1}{2}}\cdot\bar{P}_{(n_{feed}+1)-\frac{1}{2}}}$$

$$\bar{u}_{(n_{feed}+1)-\frac{1}{2}} = \frac{\bar{u}_{feed}\bar{P}_{feed} + \bar{u}_{n_{feed}+\frac{1}{2}}\bar{P}_{n_{feed}+\frac{1}{2}}}{\bar{P}_{(n_{feed}+1)-\frac{1}{2}}}$$

Again, the values of $\bar{P}_{(n_{feed}+1)-\frac{1}{2}}$, $\bar{u}_{n_{feed}+\frac{1}{2}}$ and $y_{i,n_{feed}+\frac{1}{2}}$ are obtained from Eqs. (B.1-B.3).

https://doi.org/10.1016/j.ces.2019.03.055

References

Baines, M. J., 1994. Moving Finite Elements. Oxford University Press, Inc., New York, NY, USA.

Bhatt, T. S., Sliepcevich, A., Storti, G., Rota, R., 2014. Experimental and modeling analysis of dual-reflux pressure swing adsorption process, Industrial and Engineering Chemistry Research 53(34), 13448-13458.

Bhatt, T. S., Storti, G., Denayer, J. F. M., Rota, R., 2017. Optimal design of dual-reflux pressure swing adsorption units via equilibrium theory: Process configurations employing heavy gas for pressure swing, Chemical Engineering Journal 311, 385-406.

Bhatt, T. S., Storti, G., Rota, R., 2015. Detailed simulation of dual-reflux pressure swing adsorption process, Chemical Engineering Science 122, 34-52.

Bhatt, T. S., Storti, G., Rota, R., 2013. Optimal design of dual-reflux pressure swing adsorption units via equilibrium theory, Chemical Engineering Science 102, 42-55.

Casas, N., Schell, J., Joss, L., Mazzotti, M., 2013. A parametric study of a PSA process for pre-combustion CO2 capture, Separation and Purification Technology 104, 183-192.

Coimbra, M., Rodrigues, A., Rodrigues, J., Robalo, R., Almeida, R., 2016. Moving Finite Element Method. Boca Raton: CRC Press.

Diagne, D., Goto, M., Hirose, T., 1995. Experimental study of simultaneous removal and concentration of CO2 by an improved pressure swing adsorption process, Energy Conversion and Management 36(6-9), 431-434.

Diagne, D., Goto, M., Hirose, T., 1994. New PSA process with intermediate feed inlet position operated with dual refluxes: Application to carbon dioxide removal and enrichment, Journal of Chemical Engineering of Japan 27(1), 85-89.

Ebner, A. D., Ritter, J. A., 2004. Equilibrium theory analysis of dual reflux PSA for separation of a binary mixture, AIChE Journal 50(10), 2418-2429.

Ebner, A. D., Ritter, J. A., 2002. Equilibrium theory analysis of rectifying PSA for heavy component production, AIChE Journal 48(8), 1679-1691.

Farooq, S., Ruthven, D., Boniface, H., 1989. Numerical simulation of a pressure swing adsorption oxygen unit, Chemical Engineering Science 44(12), 2809-2816.

Fox, R. O., 1996. Computational methods for turbulent reacting flows in the chemical process industry, Revue de l'Institute Francais du Petrole 51(2), 215-243.

Friedrich, D., Ferrari, M. -., Brandani, S., 2013. Efficient simulation and acceleration of convergence for a dual piston pressure swing adsorption system, Industrial and Engineering Chemistry Research 52(26), 8897-8905.

https://doi.org/10.1016/j.ces.2019.03.055

Grande, C. A., Blom, R., 2012. Dual pressure swing adsorption units for gas separation and purification, Industrial and Engineering Chemistry Research 51(25), 8695-8699.

Haghpanah, R., Majumder, A., Nilam, R., Rajendran, A., Farooq, S., Karimi, I. A., Amanullah, M., 2013. Multiobjective optimization of a four-step adsorption process for postcombustion CO2 capture via finite volume simulation, Industrial and Engineering Chemistry Research 52(11), 4249-4265.

Hoffman, J. D., Frankel, S., 2001. Numerical Methods for Engineers and Scientists. : CRC press.

Kearns, D. T., Webley, P. A., 2006a. Modelling and evaluation of dual reflux pressure swing adsorption cycles: Part II. Productivity and energy consumption, Chemical Engineering Science 61(22), 7234-7239.

Kearns, D. T., Webley, P. A., 2006b. Modelling and evaluation of dual-reflux pressure swing adsorption cycles: Part I. Mathematical models, Chemical Engineering Science 61(22), 7223-7233.

LeVeque, R. J., 2002. Finite Volume Methods for Hyperbolic Problems. : Cambridge university press.

Li, D., Zhou, Y., Shen, Y., Sun, W., Fu, Q., Yan, H., Zhang, D., 2016. Experiment and simulation for separating CO2/N2 by dual-reflux pressure swing adsorption process, Chemical Engineering Journal 297, 315-324.

Liao, H. -., Shiau, C. -., 2000. Analytical solution to an axial dispersion model for the fixed-bed adsorber, AIChE Journal 46(6), 1168-1176.

May, E. F., Zhang, Y., Saleman, T. L. H., Xiao, G., Li, G. K., Young, B. R., 2017. Demonstration and optimisation of the four Dual-Reflux Pressure Swing Adsorption configurations, Separation and Purification Technology 177, 161-175.

Mc Intyre, J. A., Holland, C. E., Ritter, J. A., 2002. High enrichment and recovery of dilute hydrocarbons by dual-reflux pressure-swing adsorption, Industrial and Engineering Chemistry Research 41(14), 3499-3504.

Mcintyre, J. A., Ebner, A. D., Ritter, J. A., 2010. Experimental study of a dual reflux enriching pressure swing adsorption process for concentrating dilute feed streams, Industrial and Engineering Chemistry Research 49(4), 1848-1858.

Ruthven, D. M., 1984. Principles of Adsorption and Adsorption Processes. John Wiley & Sons.

Saleman, T. L., Li, G. K., Rufford, T. E., Stanwix, P. L., Chan, K. I., Huang, S. H., May, E. F., 2015. Capture of low grade methane from nitrogen gas using dual-reflux pressure swing adsorption, Chemical Engineering Journal 281, 739-748.

Shafeeyan, M. S., Wan Daud, W. M. A., Shamiri, A., 2014. A review of mathematical modeling of fixed-bed columns for carbon dioxide adsorption, Chemical Engineering Research and Design 92(5), 961-988.

Sholl, D. S., Lively, R. P., 2016. Seven chemical separations to change the world, Nature 532(7600), 435-437.

https://doi.org/10.1016/j.ces.2019.03.055

Sivakumar, S. V., Rao, D. P., 2011a. Modified duplex PSA. 1. sharp separation and process intensification for CO2-N2-13X zeolite system, Industrial and Engineering Chemistry Research 50(6), 3426-3436.

Sivakumar, S. V., Rao, D. P., 2011b. Modified duplex PSA. 2. sharp separation and process intensification for N2-O2-5A zeolite system, Industrial and Engineering Chemistry Research 50(6), 3437-3445.

Skarstrom, C. W., 1959. USE OF ADSORPTION PHENOMENA IN AUTOMATIC PLANT-TYPE GAS ANALYZERS, Annals of the New York Academy of Sciences 72(13), 751-763.

Thakur, R. S., Kaistha, N., Rao, D. P., 2011. Process intensification in duplex pressure swing adsorption, Computers and Chemical Engineering 35(5), 973-983.

Tian, C., Fu, Q., Ding, Z., Han, Z., Zhang, D., 2017. Experiment and simulation study of a dual-reflux pressure swing adsorption process for separating N2/O2, Separation and Purification Technology 189, 54-65.

Webley, P. A., He, J., 2000. Fast solution-adaptive finite volume method for PSA/VSA cycle simulation; 1 single step simulation, Computers and Chemical Engineering 23(11-12), 1701-1712.

Yoshida, M., Ritter, J.A., Kodama, A., Goto, M., Hirose, T., 2003. Enriching reflux and parallel equalization PSA process for concentrating trace components in air, Industrial and Engineering Chemistry Research 42, 1795-1803.

Zhang, Y., Saleman, T. L. H., Li, G. K., Xiao, G., Young, B. R., May, E. F., 2016. Non-isothermal numerical simulations of dual reflux pressure swing adsorption cycles for separating N2 + CH4, Chemical Engineering Journal 292, 366-381.

Zhang, Y., Saleman, T. L. H., May, E. F., Young, B. R., 2014. A numerical modelling approach for dual reflux PSA separation of N2 and CH4 in LNG production, Computer Aided Chemical Engineering 33, 103-108.

Zou, Y., Xiao, G., Li, G., Lu, W., May, E. F., 2017. Advanced non-isothermal dynamic simulations of dual reflux pressure swing adsorption cycles, Chemical Engineering Research and Design 126, 76-88.

https://doi.org/10.1016/j.ces.2019.03.055